applied optics

Analysis of focused laser differential interferometry

B. E. Schmidt* and J. E. Shepherd

California Institute of Technology, 1200 E. California Blvd., Pasadena, California 91125, USA
**Corresponding author: bryan.e.schmidt@gmail.com*

Received 10 July 2015; revised 31 August 2015; accepted 2 September 2015; posted 3 September 2015 (Doc. ID 245742); published 30 September 2015

A computational method for predicting the output of a focused laser differential interferometer (FLDI) given an arbitrary density field is presented. The method is verified against analytical predictions and experimental data. The FLDI simulation software is applied to the problem of measuring Mack-mode wave packets in a hypervelocity boundary layer on a 5° half-angle cone. The software is shown to complement experiments by providing the necessary information to allow quantitative density fluctuation magnitudes to be extracted from experimental measurements.

OCIS codes: (120.3180) Interferometry; (000.2170) Equipment and techniques; (000.4430) Numerical approximation and analysis; (140.0140) Lasers and laser optics.

http://dx.doi.org/10.1364/AO.54.008459

1. INTRODUCTION

Focused laser differential interferometry is a promising technique for measuring density disturbances in supersonic and hypersonic flows, particularly in measuring boundary-layer instabilities. Focused laser differential interferometry is a subset of laser differential interferometry, a field with many examples in the literature, e.g., [1–3] and others. Texts that describe the general principles of interferometry and describe several types of interferometers are abundant, e.g., [4]. The focused laser differential interferometer (FLDI) was first described by Smeets [5] where it was used to measure density fluctuations in wind tunnel flows and turbulent jets in a desktop-type experiment. The technique was limited in its usefulness at that time because of limitations on photodetectors and data acquisition systems as well as the availability of suitable lasers. Parziale revitalized the technique in 2013 [6–8] to measure instabilities in a hypervelocity boundary layer on a slender body in the T5 hypervelocity tunnel at Caltech and to make measurements of the free stream environment in T5 [9]. This paper will develop some general results for the FLDI but will concentrate on the application of measuring second-mode (Mack) waves in hypersonic boundary layers [10].

The FLDI is a very attractive instrument for making such measurements for several reasons. It has high frequency response of greater than 10 MHz, spatial resolution of the order of hundreds of microns in the streamwise direction, and a high signal-to-noise ratio. Additionally, because of the focusing ability of the FLDI, it rejects much of the unwanted signal away from the flow feature of interest near the instrument's best focus. A key advantage then is that for many flows the FLDI is largely immune to large-amplitude density disturbances created by the shear layers of a wind tunnel with a free jet inside the test section. Preliminary qualitative evidence of this property of the FLDI has been observed in experiments involving translating a small turbulent jet, e.g., Section 3.2.3 of [11]. The effect was examined in detail by Fulghum in Section 3.10.2 of [12] and is also studied in this paper.

As more researchers use the technique, it is critical to better understand how the FLDI signal is produced and how to properly analyze experimental results to extract meaningful quantitative information about the fluctuating density field in the flow. Fulghum presents a very thorough description of the FLDI technique from an aero-optical point of view and derives system transfer functions for the instrument for a few simple flow geometries [12]. This paper presents a computational method for simulating the response of the FLDI to arbitrary density fields in order to determine the sensitivity of the instrument to more complicated flows with a special emphasis on measurements in hypersonic boundary layers.

2. FLDI THEORY

The essential operating principles of the FLDI are presented here; for a more complete explanation, the reader is referred to Section 3.6 of the Ph.D. thesis by Fulghum [12]. The FLDI is a nonimaging shearing interferometer. A sketch of the instrument layout is shown in Fig. 1. The linearly polarized laser beam is expanded and sheared by a prism by a small angle σ which is placed at the focal point of a converging lens. This fixes

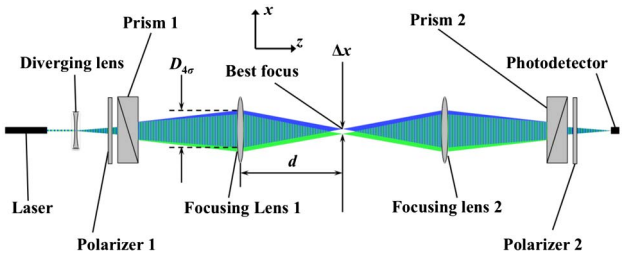

Fig. 1. Schematic of an FLDI setup. The two beams are shown as blue and green. Regions where the beams overlap are shown as striped. The coordinate system shown will be the one used throughout this paper.

the shear distance between the beams to Δx. The two beams have mutually orthogonal polarization. Wollaston prisms are the most common choice of prism in the literature, but Fulghum demonstrates great success with Sanderson prisms [13], where the divergence angle can be adjusted and the aperture can be larger so as not to truncate the expanded beam. Sanderson prisms are also generally less expensive than Wollaston prisms with small divergence angles. The choice of prism does not change the fundamental characteristics of the interferometer [14] or impact the analysis presented here. An illustration of the operation of a prism is shown in Fig. 2.

After the prism, the focusing lens brings the beams to a sharp focus. The system is symmetric about the focus so that the beams can be recombined by means of a second polarizer and the interference signal is measured by a change in intensity on a photodetector. Inhomogeneities are spatially filtered by the beams, with a much stronger filtering effect where the beam diameter is large, which makes the instrument most sensitive near the point of best focus and least sensitive close to the focusing lenses on either side of the focus, which in a free-jet wind tunnel would be close to the turbulent shear layers at the edges of the test flow. This spatial filtering effect allows the FLDI to "see through" the strong turbulence at the edges of a wind tunnel flow and measure density fluctuations of much lower intensity in the region of interest in the core of the tunnel.

As an interferometer, the FLDI is sensitive to phase differences between the two beams of the instrument. Equations describing the interference of two superimposed waves are derived in Section 7.2 of [15]. The equations in this section follow directly by considering a set of rays that are integrated over a detector. A phase difference is created by a change in the index of refraction of a transparent medium along the paths of two rays according to

$$\Delta\phi = \frac{2\pi}{\lambda}\left(\int_{s_1}^{D(\xi,\eta)} n(\underline{x}_1)\mathrm{d}s_1 - \int_{s_2}^{D(\xi,\eta)} n(\underline{x}_2)\mathrm{d}s_2\right). \quad (1)$$

Here, n is the index of refraction field through which the rays pass, the vector $\underline{x}_i$ represents the ray path parametrized by s_i, i.e., $\underline{x}_i = (x(s_i), y(s_i), z(s_i))$, $D(\xi,\eta)$ is the point on the detector where beams 1 and 2 terminate, and λ is the wavelength of the laser used. ξ and η are the coordinates on the detector face. Note that both rays terminate at the same point on the detector. Corresponding rays are separated in the test region by Δx in the x-direction, $\underline{x}_1 = \underline{x}_2 + \Delta x\hat{x}$. If the rays are interfered in an infinite fringe configuration, as they are in the FLDI, the intensity of the interfered ray at point (ξ,η) on the photodetector is given by

$$I(\xi,\eta) = I_1(\xi,\eta) + I_2(\xi,\eta) + 2\sqrt{I_1(\xi,\eta)I_2(\xi,\eta)}\cos(\Delta\phi(\xi,\eta)). \quad (2)$$

If we assume that the two rays have the same initial intensity, $I_1 = I_2 = \frac{I_0}{2}$, then Eq. (2) simplifies to

$$\frac{I(\xi,\eta)}{I_0(\xi,\eta)} = 1 + \cos(\Delta\phi(\xi,\eta)), \quad (3)$$

where $I_0(\xi,\eta)$ is the normalized intensity profile of the beam. In practice, we adjust the instrument to the middle of an interference fringe such that there is a constant phase shift of $-\pi/2$ between the two beams so that Eq. (3) can be linearized for $\Delta\phi \ll 1$ as

$$\frac{I(\xi,\eta)}{I_0(\xi,\eta)} = 1 + \sin(\Delta\phi(\xi,\eta)) \approx 1 + \Delta\phi(\xi,\eta). \quad (4)$$

The signal output by the detector $\Delta\Phi$ is proportional to the integral of Eq. (4) over the detector face D which gives the total weighted average phase change $\Delta\Phi$ as

$$\Delta\Phi = \iint_D (I(\xi,\eta) - I_0(\xi,\eta))\mathrm{d}\xi\mathrm{d}\eta = \iint_D I_0(\xi,\eta)\Delta\phi(\xi,\eta)\mathrm{d}\xi\mathrm{d}\eta. \quad (5)$$

Or, substituting Eq. (1),

$$\Delta\Phi = \iint_D (I(\xi,\eta) - I_0(\xi,\eta))\mathrm{d}\xi\mathrm{d}\eta = \frac{2\pi}{\lambda}\iint_D I_0(\xi,\eta)\left(\int_{s_1}^{D(\xi,\eta)} n(\underline{x}_1)\mathrm{d}s_1 - \int_{s_2}^{D(\xi,\eta)} n(\underline{x}_2)\mathrm{d}s_2\right)\mathrm{d}\xi\mathrm{d}\eta. \quad (6)$$

Finally, the index of refraction n in a gas is related to the density of the gas by the Gladstone–Dale relation:

$$n = K\rho + 1. \quad (7)$$

This allows the output of the FLDI to be related to the density field of the gas being probed.

The photodetector converts the total intensity to a voltage. Large phase changes ($\Delta\Phi > \pi/2$) cause phase ambiguity to

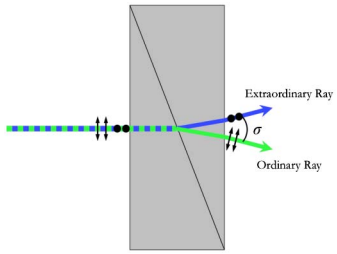

Fig. 2. Illustration of a prism (here, a Wollaston prism). The incident beam of arbitrary polarization is split into two beams by an angle σ, and the two beams at the exit have mutually orthogonal polarization. The ordinary ray is linearly polarized in the direction of beam separation and the extraordinary ray is polarized 90° from the direction of separation.

occur, as the interference wraps over several periods of light waves. Therefore, it is best to keep the phase change small enough such that the sine function can be linearized. For the FLDI, it is most useful to interpret the output not as a phase change $\Delta\Phi$ between the two closely spaced beams but rather as a finite-difference approximation to the first derivative of the phase change, $\Delta\Phi/\Delta x$. For small values of Δx, this approximates the first derivative of phase change in the direction of beam separation. Smaller values of Δx result in more accurate approximations of the derivative and therefore increased frequency response, but smaller beam separations result in lower signal magnitudes overall, which becomes an issue in practice as the electronic noise floor is approached.

The first prism (Prism 1 in Fig. 1) not only splits the light beams, but the two beams exit the prism polarized orthogonally to one another. Therefore, in order to compute the response of the instrument at the photodetector after the beams have been recombined, it is necessary to consider the state of polarization of the light along the beam paths and perform an analysis like the one in Section 3.6.1 of [12]. However, if the light is polarized at 45° relative to the separation angle of the prism before entering the first prism, the equations governing the polarization state simplify considerably. This is because each beam leaving the prism will have equal amplitude and the beams can be recombined and mixed on the detector side without explicitly using Jones vectors to combine the electric fields as long as the polarization is not rotated by the optical system. This is the configuration used by Parziale [11].

3. COMPUTATIONAL METHOD

As analytically determining the response of the FLDI instrument for a given density field is extremely difficult for all but the simplest flow geometries, a computational model of the FLDI is developed to numerically evaluate Eq. (6) for a given arbitrary density field that can vary in space and time and simulate the FLDI output. The software described in this section is referred to as the FLDI software throughout this paper. The software replicates the FLDI configuration used at Caltech [6] but can be modified to suit the dimensions of any FLDI setup. Dimensions are given in Table 1. The general procedure followed by the software is to first compute the region traversed by the FLDI beams and then to discretize the domain as described in this section. Finally, the integral in Eq. (6) is evaluated numerically along the beam paths.

The beams are assumed to have equal Gaussian intensity distributions $I_0(\xi,\eta)$ and the beams are assumed to propagate according to Gaussian beam propagation. Assuming Gaussian propagation means that the angle of paraxial rays and higher-order terms can be neglected from the full electromagnetic wave propagation equations. This is a good approximation as long as all the rays form a sufficiently small angle with the primary beam axis such that the small-angle approximation can be invoked. The validity of this assumption is examined later in this section. For a more detailed discussion of the approximations involved in assuming Gaussian beam propagation, see Chapter 4 of Born and Wolf [15].

Table 1. Optical Parameters for Simulated FLDI

Divergence angle of prisms (σ)	2 arc min
$1/e^2$ beam diameter at focusing lens ($D_{4\sigma}$)	48 mm
Focal length of focusing lenses (f)	300 mm
Distance from focusing lens to focus (d)	515 mm
λ	532 nm

The beam separation Δx is calculated by simple trigonometry to be

$$\Delta x = 2f \tan\frac{\sigma}{2} = 174.5\ \mu\text{m}. \tag{8}$$

This calculation is confirmed to be accurate by photographing the beams of the physical FLDI setup at Caltech near the best focus with a CCD camera and neutral density filters to prevent saturation.

Equations (9)–(11) can be found in Section 14.5 of [16]. The beam waist radius at the best focus w_0 is computed for Gaussian beams using Eq. (9), which is found by substitution for the divergence angle of a Gaussian beam as

$$w_0 \approx \frac{\lambda}{\pi\theta_d} \approx \frac{2\lambda d}{\pi D_{4\sigma}}. \tag{9}$$

For a diffraction-limited beam, this corresponds to a spot size of about 7 μm. The $1/e^2$ radius of the beam as a function of z, the coordinate along the beam path, is given by

$$w(z) = \sqrt{w_0^2\left(1 + \left[\frac{\lambda z}{\pi w_0^2}\right]^2\right)}, \tag{10}$$

where $z = 0$ at the beam waist.

Figure 3 shows computed beam widths near the best focus of the FLDI. For simplicity when calculating the beam profile, polar-cylindrical coordinates are used with $\hat{r}$ and $\hat{\theta}$ orthogonal to $\hat{z}$ and $r^2 = x^2 + y^2$. The normalized beam intensity cross section at a point in z is then

$$I_0(r) = \frac{2}{w^2(z)\pi}\exp\left(\frac{-2r^2}{w^2(z)}\right). \tag{11}$$

The computational domain encompassing the beams between the focusing lenses is discretized into a uniform grid of 10,300 points along the beam paths, corresponding to a dimensional step size of 100 μm which is found to be sufficient enough that the computation is not affected by the step size. Convergence is shown below in Section 4.A. The beam cross

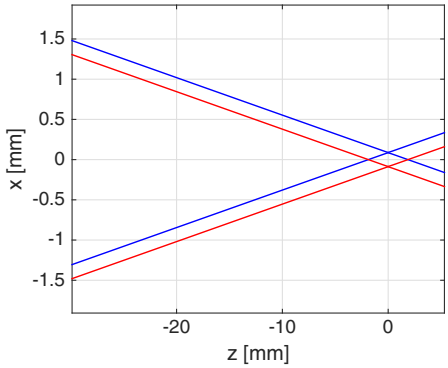

Fig. 3. Computed beam widths (out to $1/e^2$) within 30 mm of the best focus. One beam is outlined in red and the other in blue. The width of the beams at the waist is too small to see on this scale.

section is divided into a polar grid with r nondimensionalized by $w(z)$, the local $1/e^2$ beam radius. Therefore, each point (r_0, θ_0) on the polar grid at a point z_1 is on the same ray as the point (r_0, θ_0) at any other location in z. In this way the software can be considered to be performing geometric ray tracing, except the eikonal equation is not used to evaluate ray deflections due to the density field. Density perturbations are approximated as small enough (in magnitude and in extent along the ray path) that they only cause a change to the phase of each individual ray but do not cause the rays to refract significantly. The beam profiles and rays are calculated assuming a zero-disturbance field first, and then the total change in phase of the beams is calculated using an input density field. Alternatively, the method can be thought of as computing a pixelwise phase change for each beam on the face of the detector, where each grid point at a cross section in z is a pixel. Such a method is shown to produce accurate results compared to the parabolic beam method developed by White and the Rayleigh–Sommerfeld equation as long as the beam is not analyzed close to an aperture [17]. Because the polar grid is normalized by the local beam radius, integration occurs along each individual ray path instead of along the z-axis.

The polar cross-section grid extends to $r/w = \bar{r} = 2$, which contains 99.99% of the beam energy. We can now consider if assuming Gaussian beam propagation is accurate. The maximum angle formed by a beam in the domain will be the angle formed by a beam at the outer edge of the grid. Using Eqs. (9) and (10) and Table 1, the maximum ray angle is calculated to be 5.32° or 92.9 mrad. The small-angle approximation for this angle gives an error of 0.14%, hence assuming Gaussian beam propagation is clearly justified. The grid has 300 equally spaced points in the $\hat{\theta}$-direction, and grid points are chosen in the $\hat{r}$-direction such that each cell has an aspect ratio as close to 1 as possible. Points are computed starting at $\tilde{r} = 2$ inward to a specified limiting radius $\tilde{r}_0$, which is chosen to be 0.001, resulting in 363 points in $\hat{r}$. Each point is computed using the previous point according to

$$\bar{r}_k = \bar{r}_{k-1}\left(\frac{2 - \delta\theta}{2 + \delta\theta}\right), \tag{12}$$

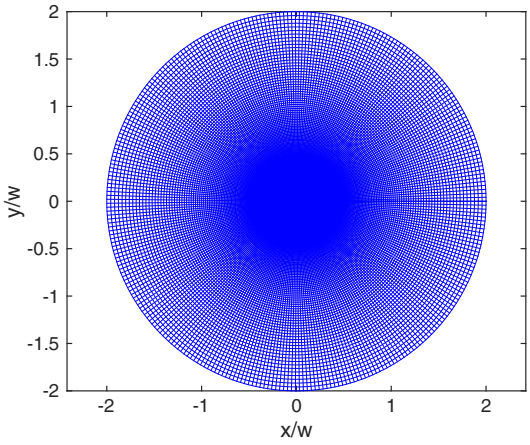

Fig. 4. Polar grid cross section nondimensionalized by the local beam waist size.

where $\delta\theta$ is the step size in the $\hat{\theta}$-direction. The grid also contains one point in the center at $\tilde{r} = 0$, bringing the total number of points at each cross-sectional grid to 108,901. The grid is shown in Fig. 4. The resolution was determined by limiting the error of numerically integrating a Gaussian using the trapezoidal rule on the grid to less than 1%.

The simulated FLDI response to an input density field $\rho(x, y, z)$ is computed by numerically evaluating Eq. (6). The integral in z is calculated using Simpson's rule and the two-dimensional integral over the face of the beam is calculated using trapezoidal integration.

4. SOFTWARE VERIFICATION

A. System Transfer Functions

It is possible to analytically derive an overall system transfer function H as a function of wavenumber for simple density disturbance fields. This is performed in detail in [12], the essence of which is summarized in this paper. Here, H is defined as the ratio of the output of the instrument to the actual first derivative of the phase field as

$$H \equiv \frac{\left(\frac{\Delta\Phi}{\Delta x}\right)_{\text{meas.}}}{\frac{\mathrm{d}\Phi}{\mathrm{d}x}}. \tag{13}$$

H for the FLDI is the convolution of two filters: one resulting from the finite beam separation approximating a derivative, and the other resulting from the Gaussian intensity distribution of the beams. In wavenumber (k) domain, these filters are simply multiplied together to give the overall $H(k)$ for the system. Here, k is the wavenumber of the density disturbance field and not the wavenumber of the laser. In general, $H(k)$ will be different for every density field geometry in (x, y, z)-space. One simple field geometry that can be analyzed analytically is a sinusoidal disturbance in x that is uniform in y and infinitesimally thin in z at $z = 0$, i.e., $n' = A\sin(kx)\delta(z)$, where A is some arbitrary disturbance amplitude and δ is the Dirac delta function. The transfer function from the Gaussian intensity distribution of the beam $H_w(k)$ can be derived from Eqs. (6), (11), and (13). We consider a detector over all space with the detector coordinates ξ and η aligned with Cartesian coordinates x and y and take the limit as the beam separation Δx approaches zero:

$$\begin{aligned}
&H_w(k)\\
&= \frac{1}{\frac{\mathrm{d}}{\mathrm{d}x}[\sin(kx)]_{x=0}} \lim_{\Delta x\to 0}\left[\frac{1}{\Delta x}\int_{-\infty}^{\infty}\int_{-\infty} I_0(x,y)\right.\\
&\left.\times\left(\int_{s_1}^{D(x,y)} \sin(kx)\delta(z)\mathrm{d}s_1 - \int_{s_2}^{D(x,y)} \sin(kx)\delta(z)\mathrm{d}s_2\right)\mathrm{d}x\mathrm{d}y\right]\\
&= \frac{1}{\frac{\mathrm{d}}{\mathrm{d}x}[\sin(kx)]_{x=0}}\int_{-\infty}^{\infty}\int_{-\infty} I_0(x,y)\frac{\mathrm{d}}{\mathrm{d}x}[\sin(kx)]\mathrm{d}x\mathrm{d}y\\
&= \frac{1}{k}\int_{-\infty}^{\infty}\int_{-\infty}\frac{2}{w^2\pi}\exp\left(\frac{-2(x^2+y^2)}{w^2}\right)k\cos(kx)\mathrm{d}x\mathrm{d}y\\
&= \exp\left(-\frac{w^2k^2}{8}\right).
\end{aligned} \tag{14}$$

At $z = 0$, this is simply

$$H_{w,0}(k) = \exp\left(-\frac{w_0^2 k^2}{8}\right). \quad (15)$$

Equation (14) reveals how the FLDI rejects an unwanted signal away from the best focus. The FLDI rapidly attenuates disturbances with wavelengths sufficiently smaller than the local beam diameter where the product of w and k is large. w is approximately linear in z away from the best focus, so a disturbance with a given wavenumber is attenuated with Gaussian decay as it moves away from the focus.

The FLDI software can compute the response for a single beam probing $k\cos(kx)$ at a beam cross section at $z = 0$ over relevant wavenumbers for disturbances in supersonic and hypersonic flows, and this is compared with the analytical result of Eq. (15) in Fig. 5. The computed response curve is nearly identical to the analytical result. The response curve is flat with a value of 1 for low wavenumbers (long wavelength) with a sharp exponential roll-off beginning at about $k = 100/\text{mm}$, which is a disturbance wavelength of 63 μm, much smaller than most relevant waves in supersonic flows. From Eq. (14) it is apparent that the roll-off point occurs at lower wavenumbers for larger beam diameters, i.e., further from the best focus. This is what makes the FLDI immune to density disturbances away from the focus, such as the turbulent shear layers at the edges of a free-jet supersonic wind tunnel.

Note, however, that since the FLDI is actually measuring a finite difference approximation to the first derivative of density along the direction of beam separation, the magnitude of the raw signal will be smallest where that derivative is smallest, i.e., at low wavenumbers. Therefore, the effect of the electronic noise floor will become significant for low wavenumber disturbances. The issue of the noise floor will be discussed later in this section.

$H_w(k)$ can also be computed analytically for a disturbance field that is uniform in z but has a finite width $2L$, i.e., $n' = A\sin(kx)(U(z+L) - U(z-L))$, where U is the Heaviside step function. This is a more physically meaningful transfer function than Eq. (15). $H_w(k)$ is simply the integral of Eq. (14) from $-L$ to L in z divided by $2L$:

$$H_w(k) = \frac{1}{2L}\int_{-L}^{L} \exp\left(-\frac{w_0^2 k^2}{8}\left(1 + \left[\frac{\lambda z}{\pi w_0^2}\right]^2\right)\right) dz$$
$$= \frac{\pi w_0\sqrt{2\pi}}{kL\lambda}\exp\left(-\frac{w_0^2 k^2}{8}\right)\text{erf}\left(\frac{kL\lambda}{2\sqrt{2}\pi w_0}\right). \quad (16)$$

Equation (16) is plotted for various values of L, the density disturbance half-width in z, in Fig. 6. As L increases, roll-off begins at lower values of k because the instrument is integrating over portions of the beam where the diameter is larger, thus filtering high wavenumber disturbances according to Eq. (14). The error function in Eq. (16) introduces a k^{-1} roll-off that extends until the Gaussian decay cuts in at a wavenumber of about $10^3/\text{mm}$.

Figures 7 and 8 compare the output of the FLDI software with the analytical result from Eq. (16) for two values of L: 10 and 30 mm. Excellent agreement is again observed between the analytical and computed transfer functions, except at high wavenumbers where numerical errors manifest away from the best focus where the beam is larger and the cross-sectional grid is therefore coarser with respect to the high wavenumber disturbances.

In addition to the filtering effect due to the changing beam size, there is a second filter due to the beams being separated by a finite distance. $H_s(k)$, the transfer function based on beam separation, is calculated by computing the response of the FLDI by approximating the FLDI as two point-detectors separated by Δx, again compared to the ideal case of the true derivative of the disturbance:

$$H_s(k) = \frac{2\sin\left(\frac{k\Delta x}{2}\right)}{\Delta x\frac{d}{dx}[\sin(kx)]_{x=0}} = \frac{2\sin\left(\frac{k\Delta x}{2}\right)}{k\Delta x}. \quad (17)$$

This is a sinc function, which has zeros for $k = \frac{2n\pi}{\Delta x}$ for integers n. This will only be true for strictly two-dimensional disturbances, which is not physical. Fulghum [12] has shown by Monte Carlo simulation that for randomly oriented disturbances the transfer function is not oscillatory and does not contain zeros. The precise form of the transfer function can in theory be determined by similar means using the FLDI software presented here, but the process is very time-consuming

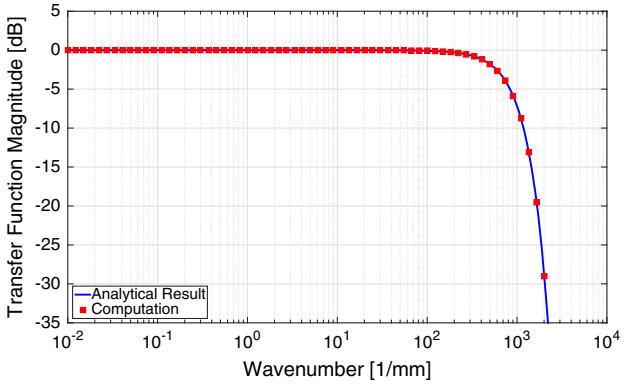

Fig. 5. Transfer function $H_w(k)$ for a single beam for 1D sinusoidal disturbances in x in an infinitesimally thin plane at $z = 0$.

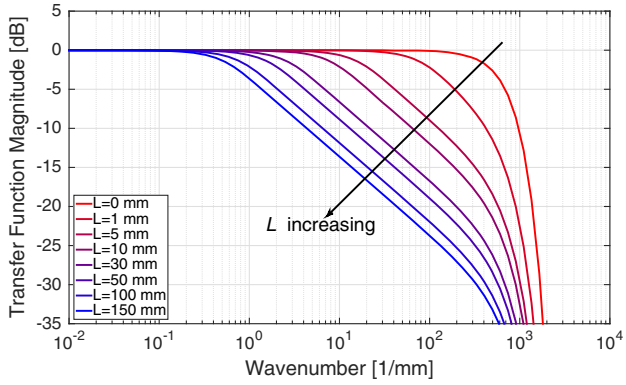

Fig. 6. Transfer function of Eq. (16) plotted for various values of L. As L increases or as more signal away from the best focus is considered, the error function in Eq. (16) contributes a k^{-1} roll-off beginning at lower values of k. This leads to attenuation of high-wavenumber disturbances away from the best focus.

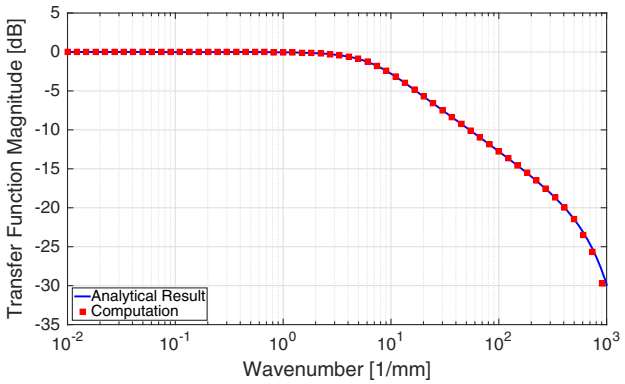

Fig. 7. Transfer function $H_w(k)$ for a single beam for uniform 2D sinusoidal disturbances in x between $z = \pm 10$ mm centered at $z = 0$.

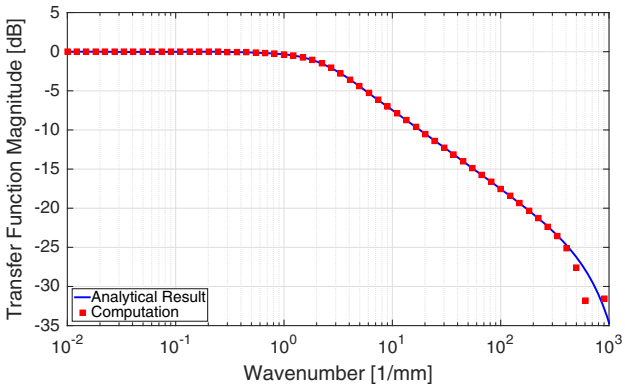

Fig. 8. Transfer function $H_w(k)$ for a single beam for uniform 2D sinusoidal disturbances in x between $z = \pm 30$ mm centered at $z = 0$.

and it has been observed that the effect from $H_w(k)$ is much more significant.

$H_w(k)$ and $H_s(k)$ are combined for strictly two-dimensional disturbances here for verification purposes because an overall transfer function can be derived analytically. Because the transfer functions are written in wavenumber space, the overall transfer function $H(k)$ is simply the product of $H_w(k)$ and $H_s(k)$. For instance, for density disturbances in the infinitesimal plane at the best focus, the overall transfer function is

$$H(k) = \frac{2}{k\Delta x} \sin\left(\frac{k\Delta x}{2}\right) \exp\left(-\frac{w_0^2 k^2}{8}\right). \quad (18)$$

Three overall transfer functions for $L = 0$ mm (infinitesimal plane at the best focus), $L = 10$ mm and $L = 30$ mm, respectively, are shown in Figs. 9–11. Excellent agreement is observed between the FLDI software (points in Figs. 9–11) and the analytical functions (lines in Figs. 9–11), affirming the accuracy of the computational method. The apparent oscillations in the transfer functions result from the sinc filter because of the strictly two-dimensional nature of the disturbance field simulated. It is also worth noting here that there is no filtering effect resulting from the overlap of the beams away from the best focus as can be seen in Fig. 3. In other words,

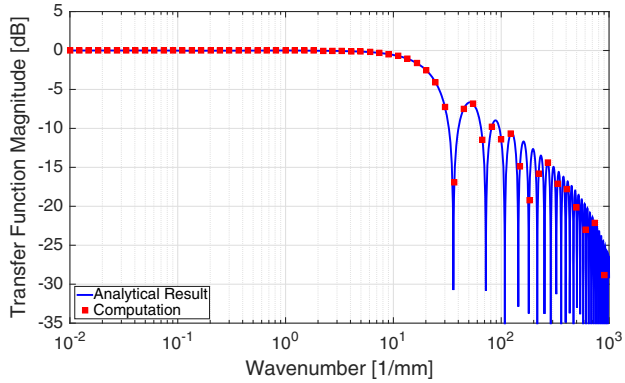

Fig. 9. Transfer function $H(k)$ for the two-beam FLDI for 1D sinusoidal disturbances in x in an infinitesimally thin plane at $z = 0$.

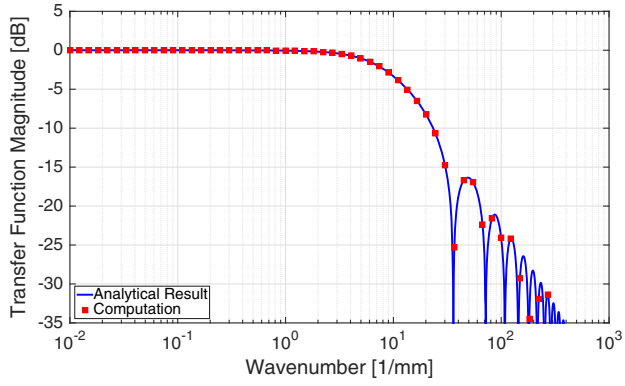

Fig. 10. Transfer function $H(k)$ for the two-beam FLDI for uniform 2D sinusoidal disturbances in x between $z = \pm 10$ mm centered at $z = 0$.

the FLDI does not reject signals by "common-mode" rejection because the beams overlap away from the best focus, but because the beam diameter is large compared to the wavelengths of the disturbances being measured. The fact that the beams overlap in space is irrelevant to signal rejection.

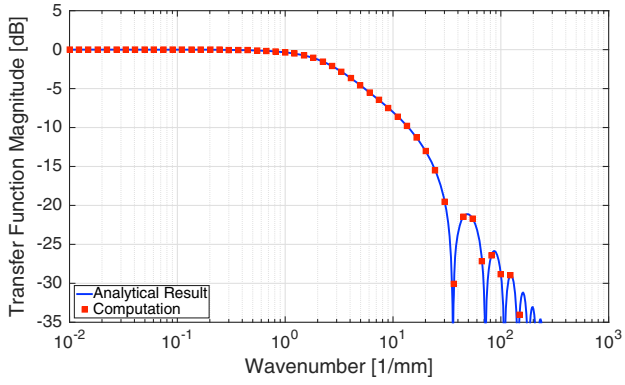

Fig. 11. Transfer function $H(k)$ for the two-beam FLDI for uniform 2D sinusoidal disturbances in x between $z = \pm 30$ mm centered at $z = 0$.

A convergence study was performed by computing the total sum-of-squares error for the transfer function shown in Fig. 11 as a function of the resolution in z, the direction of mean beam propagation. This is shown in Fig. 12 with the red square indicating the chosen resolution. Absolute error is chosen over relative error because the small absolute errors at small values of the transfer function at high wavenumbers are not important to the output of the software, but these dominate the relative error. The grid is converged with approximately 4000 points in z, corresponding to a step size of 257.5 μm. The chosen step size of 100 μm is therefore sufficiently small.

The issue of the electronic noise floor can best be seen here. Figure 13 shows the absolute response of the instrument for a disturbance propagating between ±10 mm on either side of the focus in terms of intensity due to a difference in phase change, which is converted to voltage by the photodetector. The density field is the same as that used to compute the transfer function of Fig. 10. Although the FLDI can accurately measure the derivative of a density field at wavenumbers below the roll-off, the magnitude of the output signal decreases on either side of the roll-off point. Evaluating the magnitude of density disturbances from an FLDI signal necessarily involves integration to counteract the differentiation performed by the instrument. This resolves the issue of the output signal being lower for low wavenumbers, but one must be aware of this issue in order to avoid the electronic noise floor of the physical FLDI system.

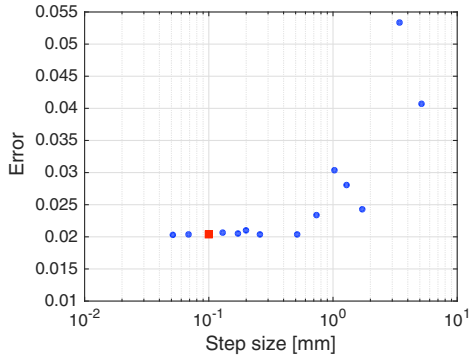

Fig. 12. Convergence study for the transfer function shown in Fig. 11. The red square indicates the chosen resolution.

B. Comparison with Experiment

An experiment with a controlled density gradient was devised to compare the FLDI software against experimental data. A gravitationally stabilized argon jet with a high aspect ratio, rectangular cross section is probed with the beams of the FLDI experimentally, and a model of the resulting density field is input into the FLDI software so that the results can be compared. The experimental apparatus is shown in Fig. 14. The primary component is a rectangular cavity of length 165 mm, width 10 mm, and depth 152 mm. Argon is fed through the hole at the bottom of the chamber at a specified pressure using a needle valve. The chamber is filled with 20–40 mesh size (approximately 400–800 μm diameter) corn cob abrasive media to ensure the flow at the exit of the chamber is laminar and uniform across the exit plane. The top of the chamber is covered with a woven-wire steel cloth with 230-by-230 μm openings to contain the abrasive media.

The jet was imaged using schlieren visualization and is found to achieve the stable configuration shown in Fig. 15. The argon is moving vertically upward at the chamber exit with an average velocity of 0.22 m/s, computed from the measured flow rate delivered by a King Instruments rotameter, but stops and reverses direction due to gravity. The maximum height achieved at $y = 0$ is determined by the flow rate and is typically about 15 mm. A two-dimensional planar computation was performed using OpenFOAM with the rhoReactingFoam solver [18]. Figure 16 shows the steady-state result of the computation, with velocity vectors on the left and streamlines on the right with both superimposed on a contour plot of argon mass fraction. Numerical schlieren from the computation exhibits qualitative agreement with the schlieren image in Fig. 15.

The flow is observed to be uniform along the length of the chamber in the z-direction, stable in time, and laminar. The chamber is placed in the test section of the Caltech Ludwieg Tube and made parallel to the z-axis of the FLDI beams by using a level suspended between two parallel circular cavities.

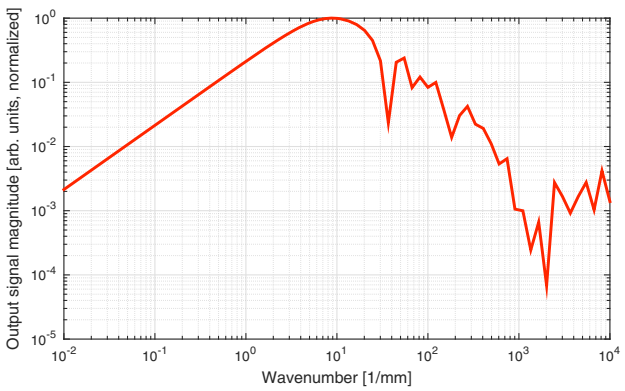

Fig. 13. Normalized FLDI output signal for sinusoidal disturbances within ±10 mm of the focus in z, corresponding to the transfer function plotted in Fig. 10.

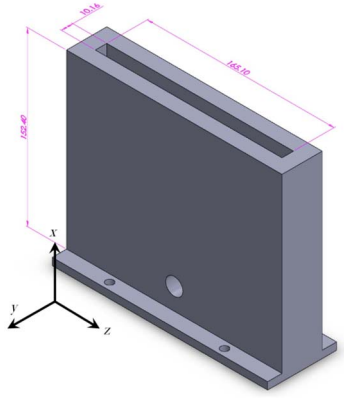

Fig. 14. Solid model of the chamber for the argon jet with dimensions given in mm. The coordinate system shown corresponds to the orientation of the coordinate system of the FLDI beams.

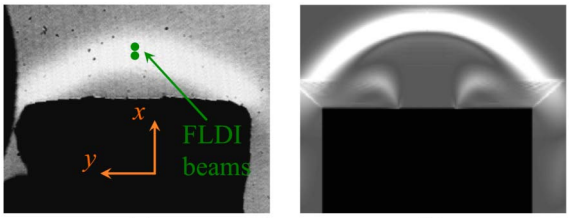

Fig. 15. (a) Schlieren image of the argon jet in the x–y plane. The top of the jet is about 15 mm from the chamber exit and is observed to be uniform across the jet cross section, temporally stable, and laminar. (b) Pseudo-schlieren image of the argon jet showing the vertical gradient in density for comparison with the experiment.

The FLDI beams are separated in the x-direction and located at the interface of the argon and air, such that they measure the density change across the interface as shown in Fig. 15(a). The resulting phase change is less than $\pi/2$, so the small-angle approximation can be invoked as in Section 2. Portions of the jet can be covered with tape such that only sections of the jet are active. Fluctuations in the ambient air are negligible compared to the density difference across the interface. The optical index field can therefore be approximated for computational purposes as varying in x and being uniform in y and z over the portion(s) where the chamber exit is not covered and uniform everywhere else, i.e., $n' = n_{\text{jet}}(x)(U(z_0 + L/2) - U(z_0 - L/2))$. This allows for comparison between the FLDI software and experiment for a number of different configurations. At each condition, the flow rate of the argon is adjusted to produce the maximum FLDI signal, meaning that the beams are centered on the maximum of the density gradient. Test cases performed are presented in Table 2 by total length of the jet in z (L_{jet}) and the center of the jet in z (z_0) (units in mm).

The variation in index of refraction in the x-direction across the argon–air interface is shown in Fig. 17. Cubic spline interpolation is used in the FLDI software when evaluating the index of refraction on the computational grid. The index of refraction for a mixture of gases is calculated from Eq. (19),

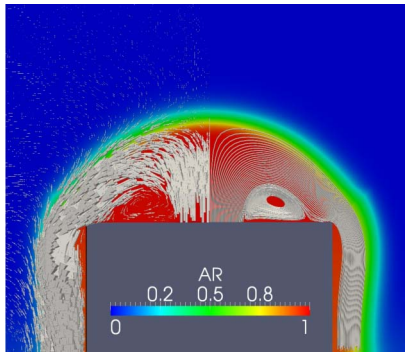

Fig. 16. Steady-state result of the OpenFOAM computation of the flow out of the argon jet. Velocity vectors are shown on the left and streamlines on the right. Both are superimposed on a contour plot of argon mass fraction. L_{jet} is the length out of the page (in the z-direction) that the cross section shown here extends.

Table 2. Argon Jet Configurations Tested

Configuration	L_{jet}	z_0
A	165	0
B	130	0
C	110	0
D	90	0
E	70	0
F	50	0
G	30	0
H	20	0
I	10	0
J	82.5	41.25
K	20	10
L	20	20
M	20	30
N	32.5	66.25

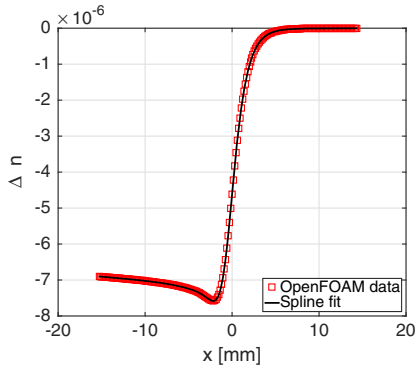

Fig. 17. Index of refraction field from the OpenFOAM computation with spline interpolation.

which is derived from Eq. (B29) in [19] by substituting the definition of mass fraction (Y):

$$n' = Y_{\text{Ar}}(\rho_{\text{Ar}} + \rho_{\text{air}})(K_{\text{Ar}} - K_{\text{air}}) + K_{\text{air}}(\rho_{\text{Ar}} + \rho_{\text{air}} - \rho_{\text{air}}|_{x\to\infty}). \quad \textbf{(19)}$$

The computational and experimental FLDI phase change outputs for each case in Table 2 are plotted versus one another in Fig. 18. Uncertainty in the experiment is difficult to quantify, but errors are believed to be largely due to three-dimensional effects at the ends of the jet. The error bars in Fig. 18 are a bound on the error from calculating the response with an additional 5 mm of jet length on either side of the jet for each configuration. Three-dimensional effects have a larger influence on shorter jet lengths, which explains the scatter in the data at the low-response end of the figure. A linear regression analysis was carried out to test the correlation of experimental data and numerical results. The regression line has a slope of 0.99 and an intercept of 0.00, compared to the ideal values of 1 and 0 for slope and intercept, respectively, and all but one of the individual points lie on the regression line within the computed uncertainty. The FLDI software can therefore be considered verified versus analytical calculations and validated against experimental data with a high degree of confidence.

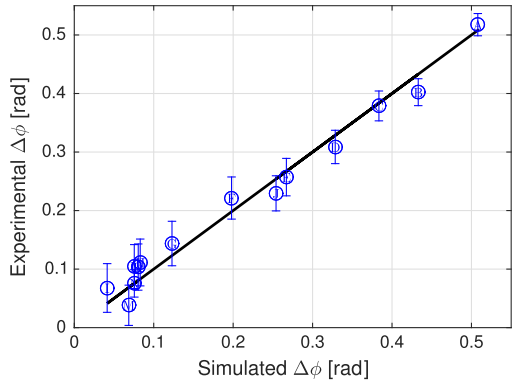

Fig. 18. Experimental versus numerical data for the argon jet experiments detailed in Table 2. The letters marking each data point correspond to the configurations in Table 2. The line is the ideal line $y = x$.

5. SIMULATED MEASUREMENTS

A. Description

One of the more promising applications of the FLDI is measuring instability waves in hypervelocity boundary layers where other more conventional techniques such as surface-mounted pressure transducers or hot-wire anemometry are not suitable. The FLDI is capable of making such measurements because of its high temporal resolution and ability to reject signals away from the best focus. This was done by Parziale at Caltech in his Ph.D. thesis [11]. These instability waves are Mack-mode waves and propagate two-dimensionally in the mean flow direction. Because the waves are two-dimensional, one can assume that waves only propagate along the x-axis of the FLDI. As such, the FLDI is quite capable of measuring their frequency, but because of the path-integrated nature of FLDI measurements it is impossible to determine their amplitude from the FLDI output alone. This point is possibly made clearest by Smeets himself [20]: "From the signals received [from a 2D shear layer], primarily qualitative information could be achieved, e.g., on the frequency spectra of the turbulent fluctuations near the focal point. The deduction of quantitative data on the level of local density fluctuations is only possible by means of assumptions and approximations. The accuracy of the results is, therefore, only moderate."

From Eq. (6) we see that the change in phase between the two FLDI beams, which is converted to a voltage by the photodetector, is an integrated function of the density fluctuations along the beam paths as

$$\frac{\Delta\Phi(t)}{\Delta x} = \frac{2\pi K}{\lambda \Delta x}\iint_D I_0(\xi,\eta) \times \left(\int_{s_1}^{D(\xi,\eta)} \rho'(\underline{x}_1, t)\mathrm{d}s_1 - \int_{s_2}^{D(\xi,\eta)} \rho'(\underline{x}_2, t)\mathrm{d}s_2\right)\mathrm{d}\xi\mathrm{d}\eta, \tag{20}$$

where ρ' represents the local density fluctuations. We seek the amplitude of ρ', the density fluctuation. If Δx is sufficiently small and recalling that $\underline{x}_1 = \underline{x}_2 + \Delta x\hat{x}$, we can write this equation in terms of derivatives in x instead of finite differences and approximate the two beam paths in Eq. (20) as being common:

$$s_1 \approx s_2 \approx s, \tag{21}$$

$$\rho(\underline{x}_1) \approx \rho(\underline{x}_2) + \frac{\partial\rho}{\partial x}\Delta x, \tag{22}$$

$$\frac{\mathrm{d}\Phi(t)}{\mathrm{d}x} \approx \frac{2\pi K}{\lambda}\iint_D I_0(\xi,\eta)\int_s \frac{\partial\rho'(\underline{x},t)}{\partial x}\mathrm{d}s\mathrm{d}\xi\mathrm{d}\eta. \tag{23}$$

Since the output of the FLDI is a function of time, not space, it is much more useful to take derivatives with respect to time. This conversion can be done using Taylor's hypothesis $x = c_r t$ for a constant phase speed c_r. We then have

$$\frac{\mathrm{d}\Phi(t)}{\mathrm{d}t} \approx \frac{2\pi K}{\lambda}\iint_D I_0(\xi,\eta)\int_s \frac{\partial\rho'(\underline{x},t)}{\partial t}\mathrm{d}s\mathrm{d}\xi\mathrm{d}\eta. \tag{24}$$

We can then apply the mean value theorem for integrals to the right-hand side to obtain

$$\frac{\mathrm{d}\Phi}{\mathrm{d}t} = \frac{2\pi K}{\lambda} Z\overline{\frac{\partial\rho'}{\partial t}}. \tag{25}$$

Here, $\overline{\frac{\partial\rho'}{\partial t}}$ represents the averaged value of the time derivative of ρ' over the spatial integral. Z is an unknown parameter with units of length that makes $\overline{\rho'}$ equal to the actual ρ' fluctuation in the boundary layer. It is approximately equal to the length of the region where the FLDI is probing the boundary layer, but it cannot be determined *a priori* from experimental data alone. However, Z is primarily a function of the flow geometry and can be calculated with knowledge from the FLDI software for a given geometry and used with experimental data for the same flow. It is sensitive to the spatial filtering of the FLDI as indicated in Eq. (16), so care must be taken to ensure that the wavelengths being measured are not significantly attenuated.

We can then integrate the FLDI output in time to obtain the density fluctuations as a function of time,

$$\frac{c_r}{\Delta x}\int_0^t \Delta\Phi(\tau)\mathrm{d}\tau = \frac{2\pi K}{\lambda} Z\overline{\rho'}(t), \tag{26}$$

or, solving for $\widetilde{\rho'}$,

$$\overline{\rho'}(t) = \frac{c_r\lambda}{2\pi\Delta x Z K}\int_0^t \Delta\Phi(\tau)\mathrm{d}\tau. \tag{27}$$

The integral can be evaluated using standard numerical integration methods, e.g., Simpson's rule. Alternatively, since instability waves are often analyzed in frequency space, we can write the Fourier transform in time of Eq. (27) as

$$\mathcal{F}[\overline{\rho'}] = \frac{c_r\lambda}{2\pi\Delta x Z K}\frac{1}{i\omega}\mathcal{F}[\Delta\Phi]. \tag{28}$$

The FLDI software can be used to make simulated measurements of a Mack-mode wave packet in a boundary layer, and the result of that simulation can be used to calculate a value for Z that can be used in experiments to determine the magnitude of the fluctuations. The wave packet is calculated for T5 shot number 2789. The boundary-layer edge conditions are as follows.

The FLDI measurement location is 710 mm from the tip of a 5° half-angle cone model as shown in Fig. 19. Wave packet

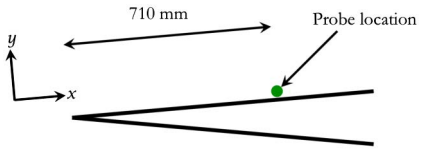

Fig. 19. Cone model used in the T5 studies.

characteristics are calculated using the method described in [21] and [22].

The density field in a hypersonic boundary layer contains a propagating disturbance that can be approximated as

$$\rho(x, y, t) = \bar{\rho}(x, y) + \rho'(x, y, t), \tag{29}$$

with a mean spatial density field $\bar{\rho}(x, y)$ and a fluctuating component ρ' representing a wave packet containing high-frequency waves representative of Mack (second-mode) instabilities, where

$$\rho' = \rho_{SF} E(x, t) \rho'^{*}. \tag{30}$$

Here, ρ_{SF} is a dimensional scale factor that determines the amplitude of the density fluctuation. It is chosen such that the maximum density fluctuation is 0.1% of the freestream value. $E(x, t)$ is an envelope describing the extent of the wave packet in x, and ρ'^{*} is a nondimensional fluctuation of the form

$$\rho'^{*} = \mathrm{Re}[g(y) \exp(i(\alpha x - \omega t))], \tag{31}$$

where g is a complex eigenfunction in y, α is a complex wavenumber containing information on both the spatial wavenumber ($\alpha_r = k$) and the spatial growth rate (α_i), and ω is the temporal frequency of the wave. Written in terms of real and imaginary parts, ρ'^{*} is given by

$$\rho'^{*} = \exp(-\alpha_i x)(g_r(y) \cos(\alpha_r x - \omega t) - g_i(y) \sin(\alpha_r x - \omega t)). \tag{32}$$

The eigenfunctions and eigenvalues were computed by Bitter [21] using parallel flow linear stability theory for a boundary layer on a cone with flow conditions given in Table 3. The real and imaginary eigenfunctions are plotted versus height above the cone surface in Fig. 20 along with the boundary layer.

From Fig. 20(c) and examination of the cone geometry it is determined that the FLDI beams are inside the boundary layer within about 10 mm on either side of the best focus. The envelope is chosen to be a Gaussian that contains about 15 wavelengths inside the region where its value is greater than 1%. Functionally, this has the form

Table 3. Boundary-Layer Edge Conditions for the T5 Shot 2789

M_e	4.55
T_e	2105 K
U_e	4191 m/s
p_e	47.1 kPa
Re/m	4.76×10^6/m
ρ_e	0.0777 kg/m^3

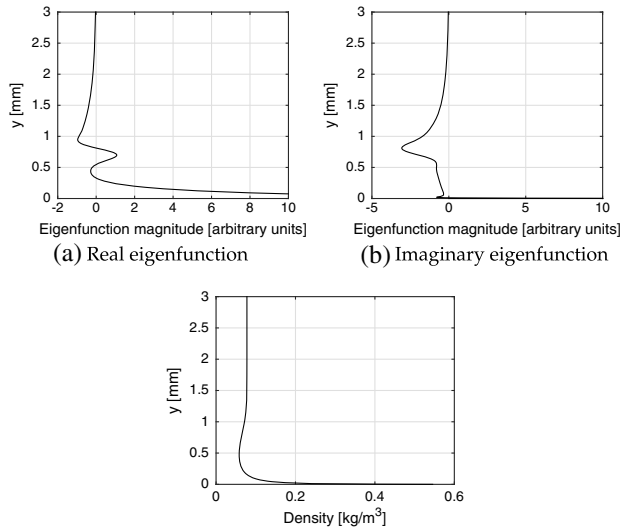

(a) Real eigenfunction (b) Imaginary eigenfunction (c) Mean density profile $\bar{\rho}(y)$

Fig. 20. (a) Real eigenfunction. (b) Imaginary eigenfunction. (c) Mean density profile $\bar{\rho}(y)$.

$$E(x, t) = \exp\left(\frac{-A(x - c_r t - x_0)^2}{l^2}\right), \tag{33}$$

for envelope length l and spatial starting location x_0.

Equation (30) has the final form of

$$\rho' = \rho_{SF} \exp\left(\frac{-A(x - c_r t - X_0)^2}{l^2} - \alpha_i x\right)(g_r(y) \cos(\alpha_r x - \omega t) - g_i(y) \sin(\alpha_r x - \omega t)). \tag{34}$$

The parameters in Eq. (34) have the values given in Table 4. It is important to recognize that we should not expect significant spatial filtering for $\alpha_r = 2.116$/mm based on Fig. 10. Note that Fig. 10 does not represent the transfer function for this cone boundary-layer flow but is the transfer function for two-dimensional disturbances propagating in x and uniform in z from $-10 < z < 10$ mm, so the exact magnitude of the transfer function at a given wavenumber is not directly applicable here. Still, Fig. 10 does predict whether or not a particular wavenumber will be appreciably attenuated.

The FLDI beams are positioned in the simulation at the local maximum of the density eigenfunction at $y = 0.81$ mm. The density fluctuations are converted to refractive index fluctuations by the Gladstone–Dale relation [Eq. (7)] with $K = 0.227 \times 10^{-3}$ m^3/kg. The wave packet is assumed to be axisymmetric with respect to the cone axis. The local density

Table 4. Boundary-Layer Wave Packet Parameters

ρ_{SF}	2.276×10^{-20} kg/m^3
A	$-\ln 0.01 = 4.6$
L	$14\pi/\alpha_r = 20.8$ mm
x_0	710 mm $- l = 689.2$ mm
c_r	3633 m/s
α_i	−0.0488/mm
$\alpha_r = k$	2.116/mm
$\omega = 2\pi f = c_r \alpha_r$	7.697×10^6 rad/s

is transformed from the FLDI coordinate system (subscript f) to a coordinate system relative to the cone surface normal (subscript c), so that Eq. (34) can be evaluated by a series of trigonometric operations for cone half-angle θ_c. Note that at $z_f = 0$, $(x_f, y_f) = (x_c, y_c)$ as expected.

$$y_c = \cos\theta_c\left(\sqrt{\left[(x_f - y_f\tan\theta_c)\tan\theta_c + \frac{y_f}{\cos\theta_c}\right]^2 + z_f^2} - \tan\theta_c(x_f - y_f\tan\theta_c)\right), \tag{35}$$

$$x_c = x_f + \tan\theta_c(y_c - y_f). \tag{36}$$

The index of refraction change, relative to the index of refraction outside the boundary layer, at a point (x_c, y_c, t) is

$$\Delta n = K(\bar{\rho}(y_c) + \rho'(x_c, y_c, t) - \rho_e). \tag{37}$$

Functions $\bar{\rho}$, g_r, and g_i are tabulated on a uniform stencil in y_c with a step size of 0.74 μm, and values are interpolated from the tabulated functions for each simulated ray in the FLDI software. The wave packet is propagated in time and the sample rate of the simulated FLDI is 20 MHz, which is sufficient to fully temporally resolve the wave packet.

B. Results

The output of the simulation is shown in Fig. 21 along with the input density disturbance at the probe location in x, which is halfway between the two FLDI beams and $z = 0$, i.e., the best focus. Note that the output is in phase change, as it would be if output from a photodetector in a physical FLDI setup, and that the output is proportional to the time derivative of the input wave packet as indicated by Eq. (27).

Equation (27) is applied to the simulated FLDI output and Z is determined by means of iteration until the peak magnitude of the measured power spectral density of the simulated output is equal to that of the input. For the flow geometry studied here, Z is calculated to be 12.6 mm. Figure 22 shows both the measured and input density fluctuations with respect to time. Note that the only difference between the two is that

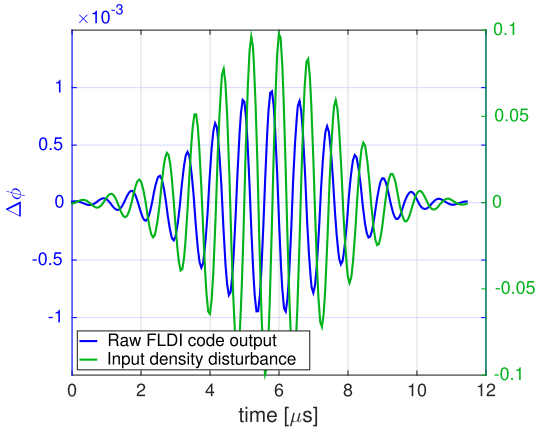

Fig. 21. Output of the FLDI simulation compared to the input boundary-layer wave packet density disturbance. The y-axis on the left corresponds to the FLDI output and the y-axis on the right corresponds to the input density at the location of the beams at $z = 0$.

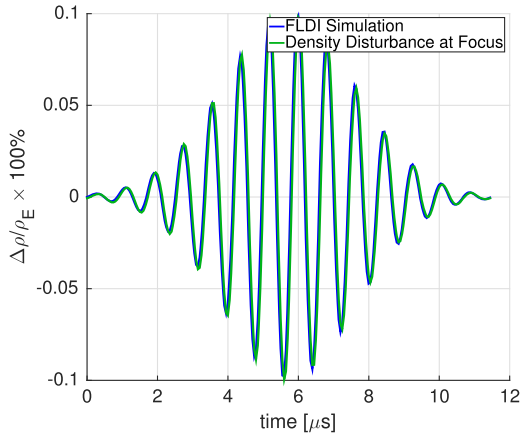

Fig. 22. Output of the FLDI simulation, scaled with Eq. (27), compared to the input boundary-layer wave packet for the optimum value of $Z = 12.6$ mm.

the measured fluctuations are slightly ahead of the input with respect to time. This is simply a consequence of the conical geometry of the flow: the wave packet will first be observed by the FLDI beams away from the focus. Equations (35) and (36) make the issue clear. For $z \neq 0$, $y_c > y_f$ so $x_c > x_f$.

Figure 23 shows the power spectral density (PSD) of the input and output density fluctuations. The two curves match each other almost exactly with the appropriate value of Z except that the simulated measurement has higher noise away from the peak in frequency. Presumably even more noise would be present in an experiment, so this slight increase in noise is inconsequential.

The parameters in Table 4, namely, α_r and c_r, are changed to determine the universality of the value of Z for wave packets of different spatial wavenumber and frequency. The values for α_r and c_r are given in Table 5 along with the computed frequency and the error in the peak amplitude of the simulated measurement relative to the peak magnitude of the input wave packet.

The error in the peak amplitude of the wave packet is appreciable only in cases 3 and 4. The reason for the large error

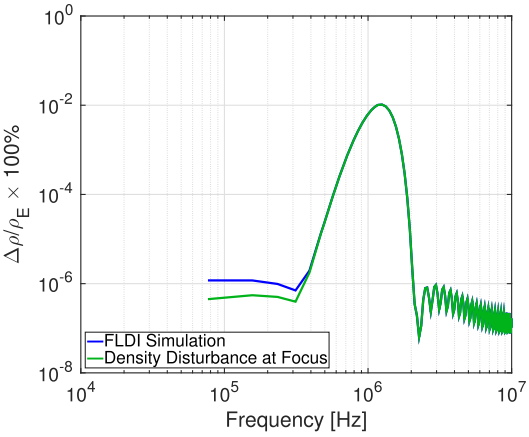

Fig. 23. PSD of the FLDI simulation, scaled with Eq. (27) and optimum Z value, compared to the PSD of the input boundary-layer wave packet.

can be deduced by examining the values of α_r in these cases and consulting Fig. 10. Recall again that the transfer functions plotted in Figs. 9–11 are not transfer functions for the conical boundary layer under examination in this section, but nonetheless they lend some insight to when the instrument will begin to roll off in wavenumber space. Notice that at $\alpha_r = 7/\text{mm}$, the transfer function has dropped to about −2 dB, which corresponds to about a 35% reduction in signal magnitude, close to the observed error in Table 5. Similarly, for $\alpha_r = 30/\text{mm}$, the transfer function is approximately equal to −17 dB, corresponding to a 98% reduction in magnitude, which is again quite close to the error in Table 5 for case 4. Physically, this means that the wavelength of the Mack-mode waves is sufficiently small enough that it is comparable in size to the beam width in the region where the FLDI is probing the boundary layer. Therefore, the waves are being heavily spatially filtered by the beams.

It is interesting to examine further the output from the FLDI software for case 4 where $\alpha_r = 30/\text{mm}$. The density change as a function of time and the power spectral density of the disturbance are shown in Fig. 24. As Table 5 indicates, the measured signal magnitude is significantly reduced compared to the input disturbance using the same value of Z calculated for case 1 where there is very little spatial filtering by the instrument. Interestingly, though, the FLDI is able to measure the frequency of the signal correctly. This is a somewhat surprising result because if one were to approximate the FLDI as two point measurements separated by the beam separation Δx, one would predict spatial aliasing if the wavenumber of the disturbance is greater than $\frac{\pi}{\Delta x}$, which would be 18 mm here. This spatial aliasing would become temporal aliasing when Taylor's hypothesis is applied. Figure 24(b) clearly does not display this behavior, so the finite beam diameter seems to prevent spatial aliasing based on wavenumber. An FLDI will only suffer from aliasing if the sampling frequency is not sufficiently high compared to the frequency of the disturbance being measured. The only effect of high wavenumbers is the attenuation of the signal due to spatial filtering, which will lead to a limitation from the electronic noise floor of the system.

Table 5. Wave Packet Properties Tested with Fixed Value of Z

Case No.	α_r [1/mm]	c_r [m/s]	f [Hz]	% Error
1	2.116	3633	1.22×10^6	0.0
2	0.4	3633	2.31×10^5	4.0
3	7	3633	4.05×10^6	−26
4	30	3633	1.73×10^7	−94
5	2.116	2500	8.42×10^5	0.0
6	2.116	5000	1.68×10^6	0.0

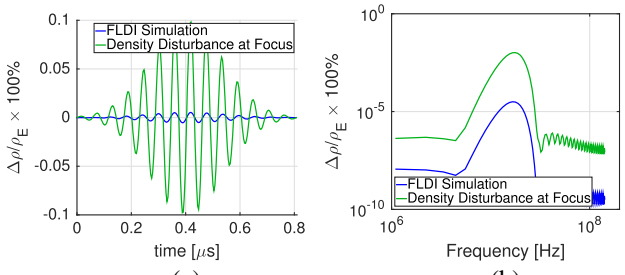

Fig. 24. (a) Output of the FLDI simulation for case 4 in Table 5 scaled with the same value of Z found in case 1 compared to the actual density disturbance at the focus. (b) Power spectral density of the FLDI simulation for case 4 compared to the PSD of the input boundary-layer wave packet at the focus.

Based on this analysis we conclude that the value of Z in Eq. (27) is only a function of the geometry of the density field being probed and the attenuation of the signal due to spatial filtering based on wavenumber. If the attenuation is sufficiently small for all wavenumbers of interest in the experiment then only a single value of Z needs to be calculated to accurately compute the density change quantitatively. Even if the wavenumbers of interest are high enough to be filtered by the FLDI, new values of Z can be calculated for given wavenumbers without much difficulty. The measurement will still be a point measurement at the focus of the FLDI and the phase speed of the disturbance must be known *a priori*, but for the specific application of measuring Mack-mode waves on a slender-body boundary layer these restrictions are not problematic. The phase speed can either be calculated from stability theory as is done here or it can be measured as in [23]. One also needs some knowledge regarding the shape of the density eigenfunctions.

To summarize, the routine to accurately compute the density change of Mack-mode waves in a hypervelocity boundary layer from FLDI data is as follows:

1. Compute wave properties and eigenfunctions from linear stability analysis, e.g., in [21].
2. Input this data into FLDI software such as the one in the current study.
3. Compute a value for Z in Eq. (27) by matching the results of step 2 to the specified density change of the input wave packet.
4. Apply Eq. (27) to the experimental FLDI data using the value of Z from step 3, taking care to ensure that the wavenumber of the Mack-mode wave is not appreciably spatially filtered by the FLDI.

The simple procedure used in [11] for computing the density disturbance magnitude for the T5 shot 2789 can give an estimate accurate within an order of magnitude if the "integration length" is estimated based on the length through which the FLDI beams are inside the cone boundary layer. However, such a procedure makes significant approximations that limit its accuracy to within about a factor of 2. The routine outlined above, on the other hand, requires knowledge of the form of the disturbances and is limited in accuracy by experimental uncertainty and any uncertainties associated with the computations performed in step 1. One could alternatively simply make an estimate of Z based on the boundary-layer geometry and skip directly to step 4 above. Estimating Z would likely give results that are more accurate than the procedure in [11] because Eq. (27) takes into account the fact that the FLDI is differentiating the density disturbance in space while the simplified procedure does not. However, the results would be less accurate than those obtained by following the full routine outlined above.

There is a caveat to these results. The freestream disturbances outside the boundary layer have been neglected in this analysis, but in an experiment the FLDI beams integrate through these disturbances and they will contribute to the output signal. Therefore, care must be taken to ensure that the freestream disturbances do not occupy the same frequency space as the disturbance of interest at the focus or that the wavenumber of the freestream disturbance at the frequency of the disturbance of interest is sufficiently high that it is heavily spatially filtered by the FLDI away from the focus. It is important to recognize that the characteristic velocity of the freestream disturbances can be different from the characteristic velocity of the disturbance of interest, as it is for hypervelocity boundary layers. Based on measurements taken in T5, it appears that the frequency range over which there is significant FLDI signal in the freestream is significantly below the 1.2 MHz of a typical Mack-mode wave packet, so signal contamination from the freestream is not expected to be problematic when using the FLDI to measure Mack-mode waves on a cone boundary layer. The effect of freestream disturbances on the output signal ought to be evaluated for each facility on a case-by-case basis for future experiments before attempting to quantify boundary-layer instability measurements to ensure the measurements are accurate. This is particularly true for low-enthalpy facilities where the frequency content of the freestream disturbances and that of Mack-mode waves are not as far apart as they are in high-enthalpy flow.

Another word of caution is warranted regarding measuring Mack-mode waves in hypervelocity boundary layers with an FLDI. From Fig. 20, it is clear that the magnitude of density fluctuations varies significantly with height in the boundary layer, and as such the output of the FLDI is quite sensitive to the location above the cone surface where the disturbance is measured. Indeed, if the measurement location is moved only 400 μm from the specified measurement location of $y = 0.81$ mm to $y = 1.2$ mm, the error in the measurement using the value of Z calculated for case 1 in Table 5 is greater than 50%. Therefore, great care must be taken to accurately measure the height of the beam centers from the model surface in an experiment.

6. CONCLUSIONS

Focused laser differential interferometry is a promising technique for measuring localized, high-frequency density disturbances in supersonic and hypersonic flows. In particular, the FLDI is an attractive instrument for measuring Mack-mode instability waves in hypersonic boundary layers. A computational tool has been developed here that has been verified against analytical predictions of the FLDI response as well as experimental measurements with a physical FLDI setup. Using the FLDI software, it is possible to calculate the output of an FLDI to an arbitrary density field. Such a prediction can only be made analytically for very simple density fields. These computations allow FLDI experiments to give quantitative measurements of the density fluctuation amplitude if certain details about the flow in question are known by applying correction factors to the computational output such that the FLDI output matches the input density disturbance of interest. This procedure is shown to work well for hypersonic boundary-layer disturbances where the disturbance is localized near the best focus of the FLDI, is two-dimensional in nature, and the phase speed of the instabilities can be accurately predicted from theory.

Some general statements can be made concerning using the FLDI to make measurements in compressible flows. The FLDI does reject signals away from its best focus, but this signal rejection is not related to common-mode rejection associated with the beams sharing common paths. The rejection is in fact attenuation due to spatial filtering because of the increasing beam diameters away from the focus. As such, disturbances with small enough wavenumbers (long enough wavelengths) will not be attenuated away from the FLDI focus and will therefore contribute to the FLDI signal over a significant extent of the beam paths. As a result, the FLDI can accurately measure the frequency content of density disturbances in a flow, but it does not in general yield information as to where along the beam path the disturbances are located or their amplitude at any given point along the beam path. In order to extract quantitative density information, details regarding the geometry of the density disturbance field, the preferred direction of the disturbances (if any), and the characteristic velocity of the disturbances must be known. If these are known, then the FLDI output can be simulated using a procedure such as the one presented here or, if the flowfield is simple enough, by analytical methods, and then experimental measurements can be adjusted as necessary such that the density fluctuation magnitude is correct. The authors are not aware of any other method to extract suitably accurate quantitative density fluctuation magnitudes from FLDI data.

Acknowledgment. The authors would like to thank Dr. Matthew Fulghum for helpful insights into how the FLDI attenuates unwanted signals. The authors would also like to thank Aditya Bhattaru for his assistance setting up the FLDI at Caltech during his Summer Undergraduate Research Fellowship in 2014. The authors would additionally like to thank Dr. Josué Melguizo-Gavilanes for performing the OpenFOAM computations in Section 4.B. Finally, the authors are very grateful to Neal Bitter for performing the boundary-layer stability calculations that provided the data for Section 5. The lead author acknowledges the support of Foster and Coco Stanback STEM Fellowship for his graduate studies.

REFERENCES

1. G. Smeets, "Observational techniques related to differential interferometry," in *11th International Conference on High Speed Photography* (Springer, 1974), pp. 283–288.
2. A. J. Laderman and A. Demetriades, "Detection of boundary-layer-transition with a laser-beam," AIAA J. **14**, 102–104 (1976).
3. M. Azzazy, D. Modarress, and T. Hoeft, "High sensitivity density fluctuation detector," J. Phys. E **20**, 428–431 (1987).
4. W. H. Steel, *Interferometry* (Cambridge University, 1967).
5. G. Smeets, "Laser interferometer for high sensitivity measurements on transient phase objects," IEEE Trans. Aerosp. Electron. Syst. **AES-8**, 186–190 (1972).
6. N. J. Parziale, J. E. Shepherd, and H. G. Hornung, "Differential interferometric measurement of instability at two points in a hypervelocity boundary layer," in *AIAA 51st Aerospace Sciences Meeting* (AIAA, 2013), paper 0521.

7. N. J. Parziale, J. E. Shepherd, and H. G. Hornung, "Differential interferometric measurement of instability in a hypervelocity boundary layer," AIAA J. **51**, 750–754 (2013).
8. N. J. Parziale, J. E. Shepherd, and H. G. Hornung, "Observations of hypervelocity boundary-layer instability," J. Fluid Mech. **781**, 87–112 (2015).
9. N. J. Parziale, J. E. Shepherd, and H. G. Hornung, "Free-stream density perturbations in a reflected-shock tunnel," Exp. Fluids **55**, 1665 (2014).
10. L. M. Mack, "Boundary-layer linear stability theory," Tech. Rep. AD-P004 046 (Jet Propulsion Laboratory and California Institute of Technology, Pasadena, CA, 1984).
11. N. J. Parziale, "Slender-body hypervelocity boundary-layer instability," Ph.D. thesis (California Institute of Technology, 2013).
12. M. R. Fulghum, "Turbulence measurements in high-speed wind tunnels using focusing laser differential interferometry," Ph.D. thesis (Pennsylvania State University, 2014).
13. S. R. Sanderson, "Simple, adjustable beam splitting element for differential interferometers based on photoelastic birefringence of a prismatic bar," Rev. Sci. Instrum. **76**, 113703 (2005).
14. M. M. Biss, G. S. Settles, and S. R. Sanderson, "Differential schlieren-interferometry with a simple adjustable Wollaston-like prism," Appl. Opt. **47**, 328–335 (2008).
15. M. Born and E. Wolf, *Principles of Optics*, 7th ed. (Cambridge University, 1999).
16. P. W. Milonni and J. H. Eberly, *Lasers* (Wiley, 1988).
17. M. D. White, "High-order parabolic beam approximation for aero-optics," J. Comput. Phys **229**, 5465–5485 (2010).
18. H. G. Weller, G. Tabor, H. Jasak, and C. Fureby, "A tensorial approach to computational continuum mechanics using object-oriented techniques," Comput. Phys. **12**, 620–631 (1998).
19. I. I. Glass and H. Kawada, "Prandtl–Meyer flow of dissociated and ionized gases," Tech. Rep. 85 (University of Toronto, 1962).
20. G. Smeets, "Flow diagnostics by laser interferometry," IEEE Trans. Aerosp. Electron. Syst. **AES-13**, 82–90 (1977).
21. N. P. Bitter and J. E. Shepherd, "Stability of highly cooled hypervelocity boundary layers," J. Fluid Mech. **778**, 586–620 (2015).
22. L. M. Mack, "Computations of the stability of the laminar compressible boundary layer," in *Methods in Computational Physics*, B. Alder, S. Fernback, and M. Rotenberg, eds. (Academic, 1965), Vol. **4**, pp. 247–299.
23. S. Laurence, A. Wagner, and K. Hannemann, "Schlieren-based techniques for investigating instability development and transition in a hypersonic boundary layer," Exp. Fluids **55**, 1782 (2014).